



Cite as  
Nano-Micro Lett.  
(2026) 18:262

Received: 10 December 2025  
Accepted: 17 January 2026  
© The Author(s) 2026

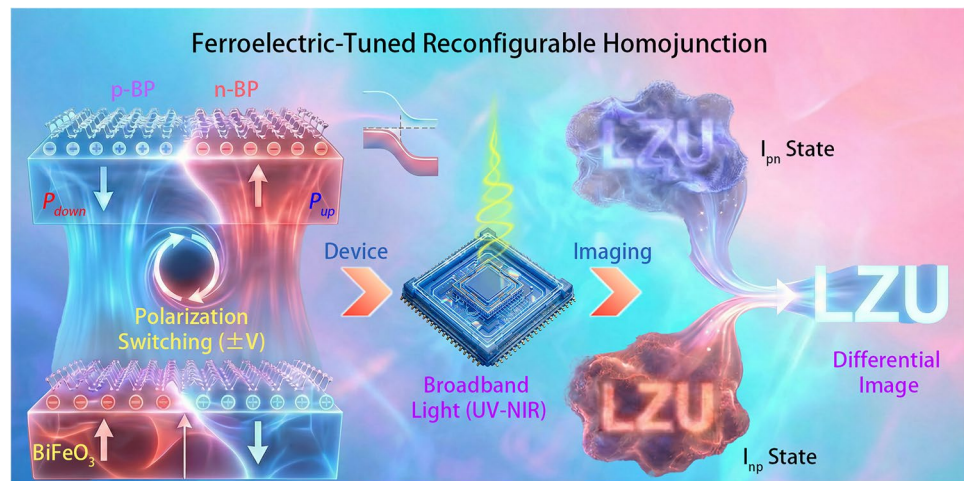
# High-Performance Differential Imaging via Reconfigurable Black Phosphorus p–n Homojunction Optoelectronics

Rui Hao<sup>1,2</sup>, Lili Luo<sup>1</sup>, Lu Yang<sup>1</sup>, Xue Yang<sup>2</sup>, Fengsong Gao<sup>1</sup>, Meijie Zhu<sup>2</sup>, Yingtao Li<sup>1</sup> ✉, Qingliang Feng<sup>2</sup> ✉, Zemin Zhang<sup>1</sup> ✉

## HIGHLIGHTS

- Ferroelectric BiFeO<sub>3</sub> gating dynamically switches the black phosphorus (BP) homojunction between p–n and n–p states, enabling non-volatile reconfiguration.
- BP/BiFeO<sub>3</sub> heterostructure achieves broadband self-powered photodetection from 365 to 1550 nm, with responsivity ranging from 44 mA W<sup>-1</sup> (808 nm) to 1.6 A W<sup>-1</sup> (425 nm) and specific detectivity up to 1.8×10<sup>12</sup> Jones.
- Differential imaging leverages reversible p–n/n–p polarity switching to cancel common-mode static noise and enhance edge detection in near-infrared imaging.

**ABSTRACT** The advancement of differential imaging and adaptive machine vision demands hardware capable of dynamic signal modulation, yet traditional photodetectors are limited by static doping profiles and fixed junction polarities. To overcome this bottleneck, we present a reconfigurable black phosphorus (BP) p–n homojunction photodetector engineered via in situ ferroelectric domain programming. By leveraging the non-volatile ferroelectric field of a bismuth ferrite substrate, we achieve



precise, nondestructive modulation of the BP band structure, allowing for reversible switching between p–n and n–p configurations within a single device channel. This ferroelectric doping strategy effectively eliminates interface damage associated with ion implantation while enabling programmable rectification behaviors. The device demonstrates self-powered operation with a responsivity of 44 mA W<sup>-1</sup> at 808 nm under zero-bias conditions. Crucially, we demonstrate a single-pixel imaging prototype where the reconfigurable junction polarity enables tunable edge sharpness and high-fidelity image reconstruction. This work establishes a paradigm for ferroelectrically programmable 2D devices, providing a versatile platform for differential imaging and contrast-enhancement optoelectronic applications.

**KEYWORDS** Ferroelectric; Reconfigurable; Black phosphorus; BiFeO<sub>3</sub>; Differential imaging

✉ Yingtao Li, ytli@lzu.edu.cn; Qingliang Feng, fengql@nwpu.edu.cn; Zemin Zhang, zhangzemin@lzu.edu.cn

<sup>1</sup> School of Physical Science and Technology, Lanzhou University, Lanzhou 730000, People's Republic of China

<sup>2</sup> School of Chemistry and Chemical Engineering, Northwestern Polytechnical University, Xi'an 710072, People's Republic of China

Published online: 28 February 2026



SHANGHAI JIAO TONG UNIVERSITY PRESS

Springer

## 1 Introduction

The shift toward intelligent machine vision requires hardware capable of “in-sensor” processing, moving beyond simple intensity detection to advanced differential imaging [1, 2]. To achieve this, optoelectronic devices must evolve from static architectures to reconfigurable systems capable of adapting to dynamic optical inputs [3–5]. Two-dimensional (2D) materials, particularly black phosphorus (BP), are uniquely suited for this challenge due to their tunable direct bandgap (0.3–2.0 eV) and high carrier mobility [6–9]. While conventional p–n junctions are static, the atomic thickness of BP allows its conductivity to be locally inverted via external fields, creating reconfigurable homojunctions within a single flake [10–12]. This ability to dynamically switch between p–n and n–p states unlocks programmable functionalities within a single device and enables sophisticated applications such as differential imaging.

However, realizing high-quality, stable, and precisely positioned p–n homojunctions in 2D materials, especially BP, remains a critical bottleneck [13]. Current doping technologies present a dilemma. “Hard” methods, such as ion implantation [14, 15] and plasma treatment [16], offer precise dopant profiling but inevitably introduce significant crystal lattice damage, which is particularly detrimental to atomically thin materials. On the other hand, “soft” strategies face their own challenges. Chemical doping via surface adsorption or substitutional doping is often unstable, non-uniform, or difficult to control [17]. Electrostatic gating, using split-gate architectures, can define clean p–n junctions, but this approach is volatile, requiring a constant power supply to maintain the doping state [18, 19].

Ferroelectric domain engineering offers a promising nondestructive pathway to induce stable, non-volatile electrostatic doping [19–22]. While recent advances utilizing organic polymers (e.g., P(VDF-TrFE)) [23] or periodically poled lithium niobate (PPLN) [24] have demonstrated the feasibility of ferroelectric-gated 2D devices, they face inherent limitations in reconfigurability and integration. Organic ferroelectrics often suffer from limited thermal stability and weaker polarization. PPLN typically relies on pre-patterned, fixed domain configurations in bulk crystals, which restricts the device to static operations. In contrast, bismuth ferrite (BFO) emerges as an ideal candidate for dynamically reconfigurable optoelectronics. BFO can be fabricated as

high-quality epitaxial thin films, allowing for seamless integration with planar device architectures [25]. More importantly, beyond its colossal remnant polarization (up to 100  $\mu\text{C cm}^{-2}$ ) and high Curie temperature (830 °C), BFO thin films allow for in situ, reversible domain switching via external voltages [26]. This unique capability enables the realization of truly programmable p–n homojunctions that can be dynamically modulated during operation, a feat not easily achievable with pre-poled bulk ferroelectrics.

In this work, we present a reconfigurable BP p–n homojunction photodetectors via BFO ferroelectric polarization for advancing differential imaging. The ferroelectric field generated by BFO induces pronounced band bending and Fermi-level modulation in BP, establishing a stable built-in electric field that enhances the separation and transport of photogenerated carriers. By reversibly switching the ferroelectric polarization direction, the BP channel can be dynamically programmed into either the p–n or n–p state. As a result, the BP homojunction exhibits clear rectifying characteristics and stable zero-bias operation, achieving a responsivity of 44  $\text{mA W}^{-1}$  at 808 nm while maintaining broadband self-powered detection from 365 to 1550 nm. TCAD simulations further confirm the ferroelectric-field-induced band modulation and carrier redistribution. Crucially, a straightforward differential imaging approach that enables high-fidelity near-infrared image reconstruction with enhanced edge definition was achieved by alternating between the p–n and n–p states. This strategy offers a general route toward reconfigurable homojunctions and provides a useful platform for self-powered optoelectronic and imaging applications.

## 2 Experimental Section

### 2.1 Preparation of Polycrystal BP

BP bulk (20 mg, > 99.999%, MK NANO, [www.mukenano.com](http://www.mukenano.com)) served as a cathode, while a Pt sheet was employed as an anode. The electrodes were set in parallel with a constant distance of 2.00 cm. Following previous reports [27, 28], tetra-*n*-butylammonium acetate (TBA·CH<sub>3</sub>COO) was dissolved in anhydrous, deoxygenated dimethylformamide to prepare the electrolyte, with a TBA·CH<sub>3</sub>COO concentration of 0.002 M. Electrochemical intercalation/exfoliation was carried out by applying a constant bias of 20.0 V for 15 min,

after which the obtained BP was collected for subsequent transfer and device fabrication.

## 2.2 Preparation of Polycrystal BFO Thin Films

Single-crystal BFO films were synthesized using pulsed laser deposition. A conductive (La,Sr)MnO<sub>3</sub> (LSMO) buffer layer was initially placed on an atomically smooth (001) SrTiO<sub>3</sub> (STO) substrate, succeeded by the epitaxial development of the BiFeO<sub>3</sub> (BFO) layer. LSMO and BFO were synthesized in an oxygen environment at 700 °C, utilizing a base vacuum of  $3 \times 10^{-3}$  Pa, with oxygen pressures of 25 Pa for durations of 10 min, respectively. Throughout the deposition, the laser fluence was sustained at  $1.2 \text{ J cm}^{-2}$  with a repetition frequency of 5 Hz. After deposition, the samples were cooled down slowly to room temperature. The resultant BFO single-crystal film exhibited a thickness of around 50 nm.

## 2.3 BP p–n Homojunction

The BP/BFO-based devices were fabricated using standard photolithography and magnetron sputtering techniques. Patterned Ti/Au electrodes with thicknesses of 20/50 nm were first deposited on the BFO substrate by photolithography, magnetron sputtering, and lift-off processes. Subsequently, few-layer BP flakes were precisely transferred onto the electrode-patterned BFO surface using a polydimethylsiloxane (PDMS)-assisted dry-transfer method.

## 2.4 Electrical and Photoelectronic Characterization

The electronic characteristics of the device were assessed by using a KEITHLEY 2612B. The incident optical power at the sample plane was calibrated using a Thorlabs PM100A optical power meter. The responsivity was calculated as  $R = I_{\text{ph}}/P_{\text{in}}$  (mA W<sup>-1</sup>). Since the beam spot fully covered the BP channel, the effective active area was defined as the BP channel area,  $A = 4 \times 10^{-6} \text{ cm}^2$ . Optical images were taken on an Olympus BX51 microscope. AFM characterization was carried out with Bruker Multimode 8 system. Raman spectra were collected using a HORIBA RRANCE SAS-LabRAM Odyssey spectrometer with a 532 nm excitation laser. The laser power at the sample was set to 15 mW, the

integration time was 10 s, and a 10× objective was used for spectral acquisition.

## 3 Results and Discussion

### 3.1 Ferroelectric Engineered Homojunction

The fabrication of a damage-free BP p–n homojunction photodetector relies on spatially modulating p- and n-type regions via the ferroelectric domains of a BFO substrate. These domains induce corresponding electron-deficient (p-type) and electron-rich (n-type) areas in the overlying few-layer BP, creating a built-in electric field that separates photogenerated carriers (Fig. 1a). The schematic structure of the few-layer BP/BFO heterojunction device is illustrated in Fig. 1b. High-quality BP nanosheets were first obtained via electrochemical exfoliation (Fig. S1) [27, 28], followed by a polydimethylsiloxane (PDMS)-assisted dry-transfer process to precisely place few-layer BP onto the BFO substrate with pre-patterned electrodes. The X-ray diffractions pattern confirms the epitaxial growth of a single-crystal BFO film with excellent phase purity (Fig. S2). Owing to the van der Waals nature of BP, no dangling bonds are present at the interface, resulting in a compact and stable heterointerface that facilitates the subsequent modulation of carrier transport in the BP channel by ferroelectric polarization. The polarization programming and characterization were carried out as schematically illustrated in Fig. S3a, b. Applying  $\pm 5$  V biases to the BFO layer reconfigures its ferroelectric polarization ( $P_{\text{up}}/P_{\text{down}}$ ), enabling programmable p–n/n–p homojunctions within the same BP channel. Figure 1c presents the piezo-response force microscopy (PFM) phase image of the BFO substrate under different polarization fields. The phase profiles extracted along the orange and blue lines (Fig. 1d) reveal a phase difference of nearly 180° between adjacent domains, confirming the complete reversibility and opposite orientations of ferroelectric polarization in BFO. The atomic force microscopy (AFM) thickness profile (Fig. 1e) indicates a layer thickness of approximately 3.5 nm, corresponding to ~7 BP layers. This thickness range ensures both stable semiconducting behavior and relatively high carrier mobility.

To directly probe the ferroelectric polarization's effect, the surface potential of BP after applying a  $\pm 5$  V bias to patterned regions was mapped (Fig. 1f). The resulting Kelvin

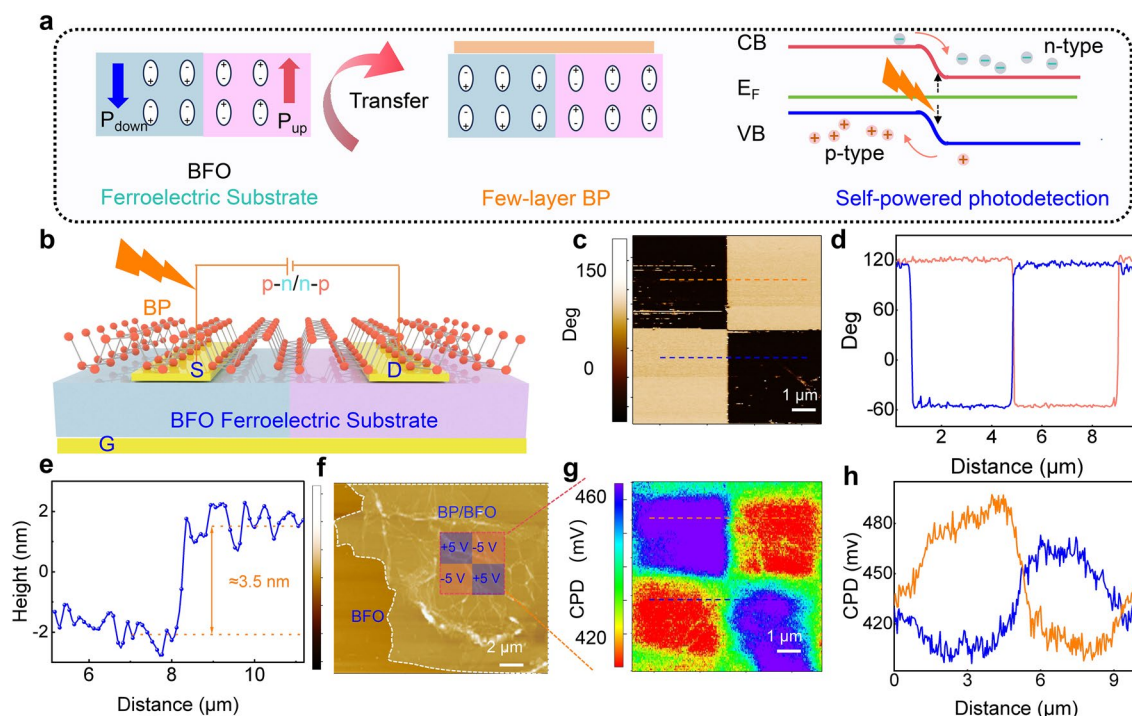


**Fig. 1** Ferroelectric Engineered Homojunction. Schematic illustration of **a** the few-layer BP p-n homojunction and **b** diagram of device structure. **c** PFM phase image of the BFO substrate under opposite polarization states and **d** corresponding phase profiles showing a 180° shift. **e–f** AFM thickness characterization of transferred BP (~3.5 nm, ~7 layers). **g** Extracted potential profiles and **h** JPFM mapping of polarized domains

probe force microscopy (KPFM) image (Fig. 1g) shows a pronounced potential contrast between BP over  $P_{\text{down}}$  and  $P_{\text{up}}$  domains. Line profiles (Fig. 1h) confirm that the surface potential decreases by 45~65 mV over  $P_{\text{down}}$  regions relative to  $P_{\text{up}}$  regions. This reversible shift stems from electrostatic modulation by polarization-bound charges at the BP/BFO interface, enabling precise control over the BP channel's carrier density and band structure. Consequently, the BFO substrate creates a controllable surface potential gradient in few-layer BP, facilitating reconfigurable p-n/n-p homojunctions.

### 3.2 In Situ Reconfiguration

Raman spectroscopy directly probes the lattice alteration in BP induced by the BFO substrate's ferroelectric polarization (Fig. 2a). The polarization field from adjacent  $P_{\text{down}}$  and  $P_{\text{up}}$  domains modulates BP's electrostatic environment, redistributing carriers and strain and thus altering its phonon vibrations. The device optical image is shown in Fig. 2b. The Raman spectrum of pristine BP (Fig. 2c) shows three

characteristic peaks:  $A_g^1$  ( $362\text{ cm}^{-1}$ ),  $B_{2g}$  ( $439\text{ cm}^{-1}$ ), and  $A_g^2$  ( $466\text{ cm}^{-1}$ ). Critically, all features of both BP and BFO ( $E_g$  and  $A_g^1$  modes in Fig. S4a) are preserved in the heterojunction (Fig. S4b), confirming that the integration process is nondestructive and maintains lattice integrity.

To probe the effect of ferroelectric polarization on BP's vibrational properties, Raman peak shifts across three regions were analyzed: intrinsic BP (unpolarized), p-type BP (on  $P_{\text{down}}$ ), and n-type BP (on  $P_{\text{up}}$ ). Despite a slight modification of the spectral shape by the BFO substrate, the three main BP modes ( $A_g^1$ ,  $B_{2g}$ ,  $A_g^2$ ) remained distinct. Notably, the elevated baseline is attributed to the optical background from the BFO substrate, as confirmed by control Raman spectra measured on bare BFO and BP/BFO under identical conditions (Fig. S4). While the  $A_g^1$  mode was stable, the  $A_g^2$  mode exhibited significant polarization-dependent shifts (Fig. 2d). Fine scanning of the  $A_g^2$  mode ( $\sim 466\text{ cm}^{-1}$ ) revealed a pronounced redshift on the  $P_{\text{down}}$  domain and a blue-shift on the  $P_{\text{up}}$  domain. Single-point spectra from the domain centers (Fig. 2e) quantified these shifts at approximately  $-1.44$  and  $+1.01\text{ cm}^{-1}$ , respectively.

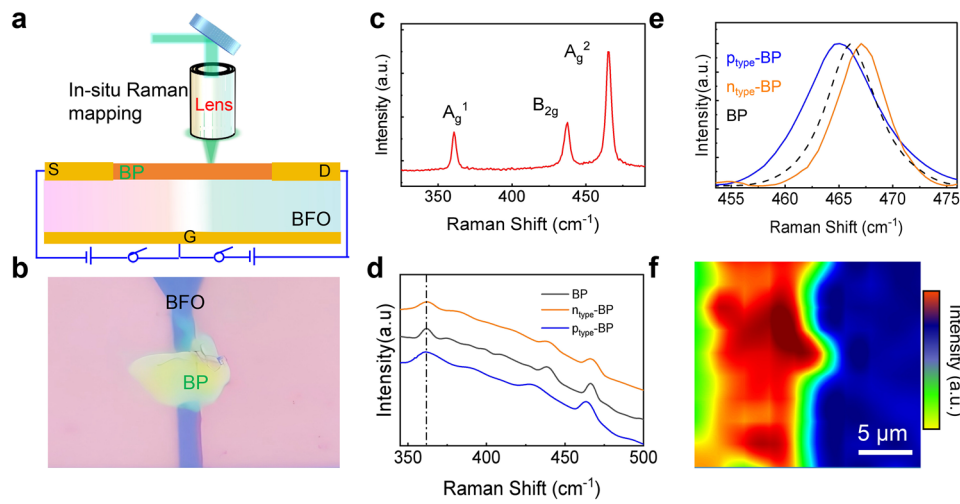


**Fig. 2** **a–b** In situ reconfiguration. Schematic illustration and optical image of the BP p–n homojunction used for in situ Raman characterization. Raman spectra of **c** BP and **d** BP on oppositely polarized BFO substrates. **e** Fine scanning of the BP  $A_g^2$  characteristic peak and **f** the corresponding Raman intensity mapping over regions with opposite ferroelectric polarization

In situ Raman mapping of this mode (Fig. 2f) spatially confirms that ferroelectric polarization electrostatically modulates both carrier type and electron–phonon coupling in BP. The observed shifts stem from BP’s strong electron–phonon coupling, where p-type doping softens the  $A_g^2$  phonon (redshift) and n-type doping stiffens it (blue-shift). These results, consistent with prior reports [29, 30], demonstrate that the BFO substrate reversibly controls the local doping in BP, directly confirming the formation of reconfigurable homojunctions.

### 3.3 Mechanism Simulations

Above analyses establish that BFO’s ferroelectric polarization reliably controls the carrier type and concentration in BP. The underlying physical mechanism, illustrated in Fig. 3a, b, involves direct electrostatic modulation of BP’s band structure. On nonpolarized BFO, BP maintains a uniform carrier profile. When contacted with oppositely polarized  $P_{down}$  and  $P_{up}$  domains, holes and electrons accumulate in the overlying BP, respectively. The resulting concentration gradients drive bidirectional carrier diffusion, establishing a space-charge region and a built-in electric field at the domain wall. This field generates a drift current that eventually balances the diffusion current at electrostatic equilibrium, aligning the Fermi levels and creating a built-in

potential. KPFM measurements confirm this potential to be  $\sim 65$  mV, directly evidencing the p–n homojunction.

To further validate the influence of ferroelectric domain polarization on carrier distribution and band alignment in BP, TCAD simulations were carried out under two representative polarization configurations. Figure 3c–i and d–i presents the electron distribution profiles corresponding to the p–n and n–p configurations, respectively. The symmetric but complementary electron concentration profiles observed under opposite polarization states confirm the controllable and reversible formation of lateral p–n/n–p junctions. The corresponding band diagrams (Fig. 3c–ii and d–ii), obtained by self-consistently solving the Poisson equation, carrier continuity equations, and drift–diffusion model, clearly illustrate the modulation of junction polarity by ferroelectric polarization. When the applied voltage is switched from  $+2/-2$  V to  $-2/+2$  V, the Fermi level shifts relative to the conduction and valence band edges of the BP channel, leading to inversion of the built-in electric field direction and a continuous transition between p–n and n–p junction configurations. Notably, asymmetric shifts in the conduction band minimum (CBM) and valence band maximum (VBM) are observed on either side of the junction, indicative of a spatial redistribution of carriers and electrostatic potential. Finally, the simulated I–V characteristics (Fig. 3c–iii and d–iii) exhibit opposite rectification, matching our experimental data and conclusively

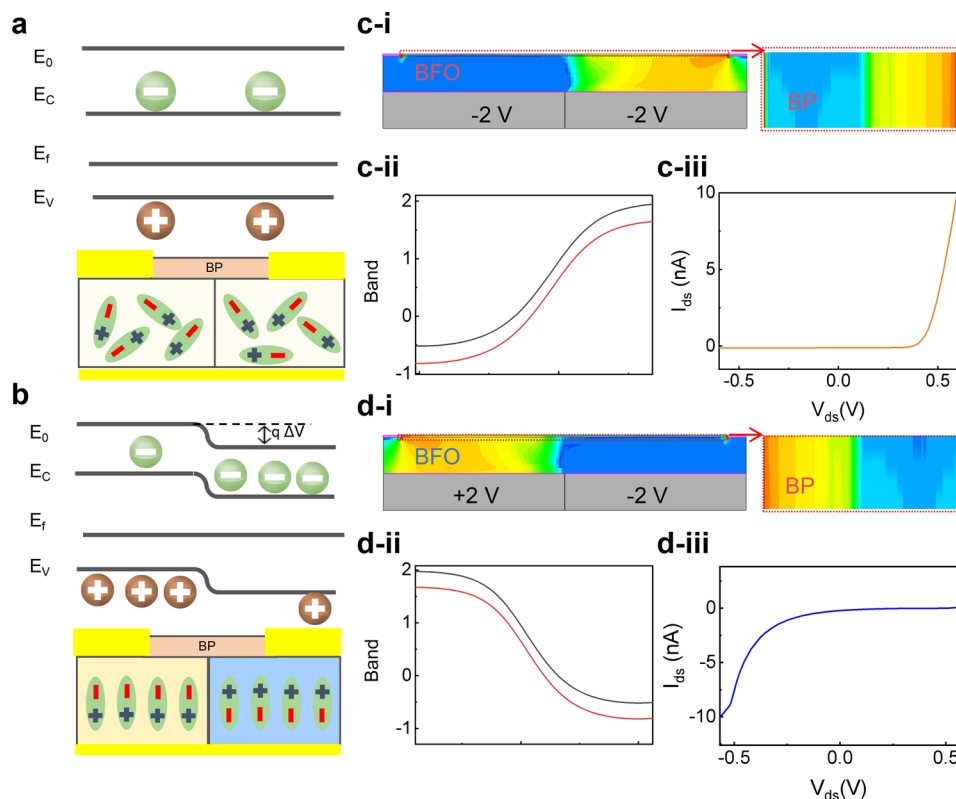


**Fig. 3** **a** Proposed mechanism of reconfigurable BP homojunctions. Nonpolarized BFO yields uniform carrier distribution, **b** while opposite ferroelectric domains induce electron–hole diffusion. **c-i**, **d-i** TCAD simulations of carrier distribution, **c-ii**, **d-ii** band diagrams, and **c-iii**, **d-iii** I–V characteristics under opposite polarizations

demonstrating that BFO polarization enables stable, programmable control over BP’s carrier polarity.

### 3.4 Reconfigurable Optoelectrical Properties

The fabricated BP exhibits excellent intrinsic electrical properties, as confirmed by output (Fig. S5) and transfer characteristics of a BP bipolar transistor (Fig. 4a). The output characteristics indicate a symmetric gate voltage-modulation behavior. A reconfigurable p–n homojunction in a single BP nanosheet was achieved by selectively polarizing the underlying ferroelectric BFO domains (the polarization-writing configuration in Fig. S3c, d). Without polarization, the BP channel shows symmetric I–V behavior. Applying a polarization voltage (+5 V, +10 V) to one electrode induces asymmetric, rectifying I–V characteristics (Fig. 4b). This occurs because the ferroelectric polarization locally controls carrier doping: a  $P_{\text{down}}$  domain p-dopes the BP, while a  $P_{\text{up}}$

domain n-dopes it. By placing the source and drain on oppositely polarized domains, we reversibly form either a p–n or n–p homojunction, as evidenced by their opposite rectification behaviors (Fig. 4c).

This ferroelectric gating also enables high-performance, self-powered photodetection. The BP/BFO device generates a broadband photoresponse from visible (365 nm) to infrared (1550 nm), with a peak responsivity at 425 nm (Fig. 4d). Under 808 nm illumination, the device exhibits rise and decay times of 0.80 and 0.61 s, respectively (Fig. 4e), and a stable, repeatable photocurrent (Figs. 4f and S6). The photocurrent scales with optical power, reaching 240 pA at the highest intensity (Fig. 4g). The dark current at 0 V bias remains stable over the measurement conditions and is  $9.16 \times 10^{-12}$  A, which is used consistently for the  $D^*$  calculations across the spectral range. Notably, the device achieves a self-powered responsivity ( $R$ ) of  $44 \text{ mA W}^{-1}$  and a specific detectivity ( $D^*$ ) of  $5.16 \times 10^{10}$  Jones at 808 nm,

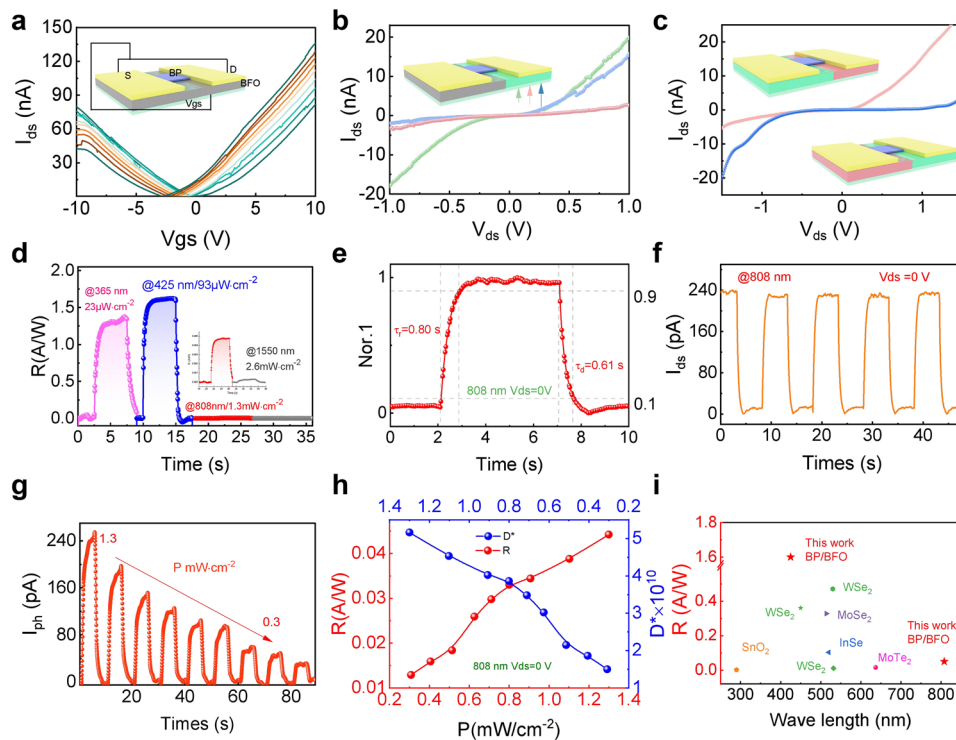


**Fig. 4** Optoelectrical characteristics of BP/BFO devices. **a** Transfer characteristic of a BP transistor. **b–c** Reversible transition from symmetric I–V behavior to rectifying p–n/n–p junctions under opposite ferroelectric polarizations. **d** Responsivity-calibrated photoresponse curves of the BP/BFO device under illumination at 365, 425, 808, and 1550 nm at 0 V bias. **e** Normalized transient photocurrent response under 808 nm illumination at 0 V bias. **f** Repeatability of I–V response under 808 nm illumination at 0 V bias. **g** Photocurrent responses under different illumination powers at 808 nm at 0 V bias. **h** Power-dependent R and  $D^*$  as functions of incident laser power density at 808 nm at 0 V bias. **i** Benchmark plots comparing the 0 V photoresponsivity with other self-powered photodetectors

and a remarkable  $1.6 \text{ A W}^{-1}$  and  $1.8 \times 10^{12}$  Jones at 425 nm (Figs. 4h and S7).

As shown in Fig. 4i and Table S2, the self-powered performance of our ferroelectric-gated BP/BFO device at 0 V bias is competitive with, and often superior to, most reported 2D material-based self-powered photodetectors [24, 31–36]. Furthermore, the photocurrent is tunable by the junction configuration, with the p–n state showing a higher photocurrent than the n–p state under identical illumination (Fig. S8). In summary, BFO’s ferroelectric polarization not only creates reversible BP homojunctions but also provides a built-in electric field for efficient, broadband, self-powered photodetection.

### 3.5 Differential Imaging

Leveraging the reversible reconfigurability of the BP/BFO heterojunction, a time-domain differential imaging

strategy was proposed to suppress background noise and enhance image contrast, as illustrated in Fig. 5a. A laser beam passes through a moving mask patterned with the characters “LZU1909” before reaching the device, and the photocurrent generated at zero bias is used to reconstruct the image (0 V bias, 808 nm,  $1.3 \text{ mW cm}^{-2}$ ). By sequentially capturing images in the high-responsivity p–n state ( $I_{p-n}$ ) and the low-responsivity n–p state ( $I_{n-p}$ ), we can extract the differential signal  $I_{\text{diff}} = |I_{p-n} - I_{n-p}|$ . This operation effectively cancels out the common-mode static noise and dark current components that are polarization-independent. Consequently, the reconstructed differential image exhibits a significantly improved signal-to-noise ratio (SNR) and clearer edge definition compared to the individual states, demonstrating the potential for hardware-level image pre-processing (Fig. 5b–d).

To quantify the spatial resolution of the differential imaging approach, an edge sharpness analysis based on the edge spread function (ESF) was performed. The steepness of the

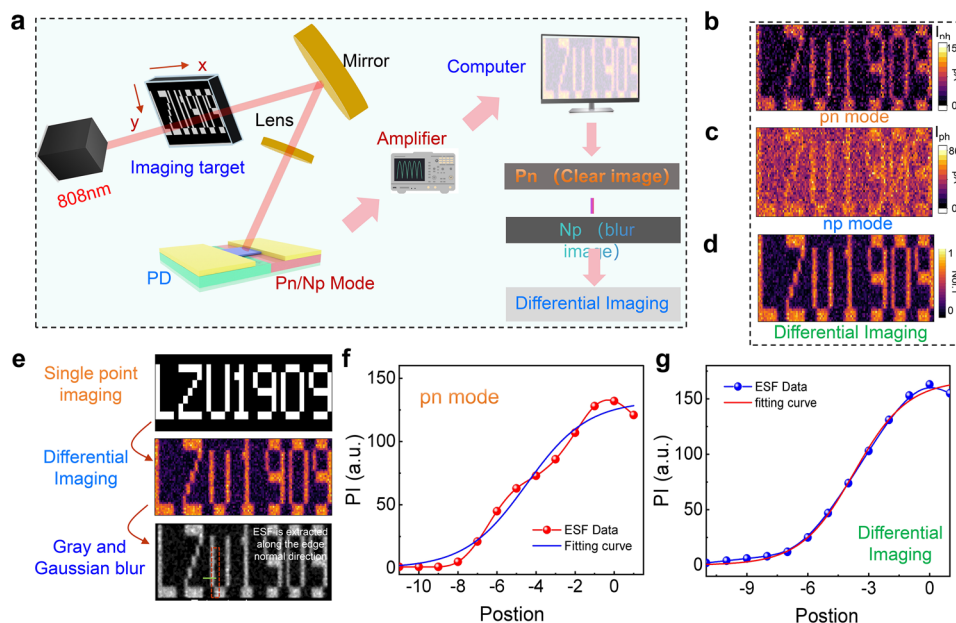


**Fig. 5** Differential imaging based on the BP homojunction device. **a** Schematic of the differential imaging scanning system using the BP homojunction device. **b, c** Single-pixel photocurrent imaging of the p–n and n–p configurations under 808 nm illumination at  $V_{ds}=0$  V and  $1.3$   $\text{mW}\cdot\text{cm}^{-2}$  power density. **d** Normalized differential image. **e** Photocurrent map generated when the laser passes through an “LZU1909” patterned mask, the corresponding differential image, and the edge-extracted result obtained by grayscale conversion, Gaussian blurring, and ESF fitting along the edge normal. **f** Local PI profiles extracted from the p–n scan and **g** the differential image, with their ESF fits

ESF reflects the system’s ability to resolve edge transitions, with a steeper slope corresponding to sharper edges. The photocurrent image used for this analysis is shown in Fig. 5e. The raw image was converted to grayscale, smoothed by Gaussian filtering, and processed by the Canny operator to extract the edge boundary. Pixel intensity (PI) profiles were then sampled along the normal direction of the edge to construct the ESF curves (Fig. 5f, g). The ESF data (orange dots) were fitted with a sigmoid function (blue curve):

$$I(x) = \frac{I_{\max}}{1 + e^{-k(x-x_0)}}$$

where  $x$  denotes the coordinate along the edge normal,  $k$  represents the slope coefficient,  $x_0$  is the edge center position, and  $I_{\max}$  is the maximum PI (0–255 for 8-bit images). For direct p–n imaging, the fitted ESF slope is  $k=0.63$  (Fig. 5f), whereas differential imaging increases the slope to  $k=0.76$  (Fig. 5g). The larger slope indicates a more abrupt edge transition, confirming that differential processing improves edge sharpness and effectively suppresses background interference.

## 4 Conclusions

In summary, we have successfully demonstrated a reconfigurable BP p–n homojunction photodetector engineered via the non-volatile ferroelectric domain programming of a BFO substrate. This in situ ferroelectric doping strategy effectively circumvents the lattice damage and instability issues associated with conventional ion implantation or chemical doping, enabling the creation of high-quality, programmable rectifying junctions within a single device channel. The fabricated device exhibits excellent self-powered performance, achieving a responsivity of  $44$   $\text{mA W}^{-1}$  and broadband detection capabilities from the visible to near-infrared regions without external bias. Furthermore, by leveraging the reversible switching between p–n and n–p configurations, we realized a single-pixel differential imaging prototype that significantly suppresses background noise and enhances edge definition. This work establishes a paradigm for ferroelectrically programmable 2D devices, providing a versatile platform for differential imaging and contrast-enhancement optoelectronic applications.

**Acknowledgements** The authors acknowledge support from the National Key Research and Development Program of China (2022YFC2204101), the National Natural Science Foundation of China (5257022607, 52272163), the Fundamental Research Funds for the Central Universities (lzujbky-2025-ytC02), the Key Research and Development Program of Gansu province (24YFGA005), and the Natural Science Basic Research Plan for Distinguished Young Scholars in Shanxi Province of China (2024JC-JCQN-13). The authors also greatly acknowledge the support of the Supercomputing Center of Lanzhou University, China.

**Author Contributions** Z.Z. and R.H. conceived and designed the experiments. R.H. and L.Y. provided the epitaxially grown BFO and BP materials and performed the ferroelectric characterizations. R.H. and L.L. fabricated the devices and carried out the electrical performance measurements. R.H., X.Y., and F.G. conducted the material characterizations. R.H. and L.L. performed the AFM and KPFM measurements. Y.L. conducted the Raman spectroscopy and TCAD simulations. R.H. and Z.Z. analyzed the data and wrote the manuscript. All authors contributed to data analysis, discussion, and manuscript revision.

#### Declarations

**Conflict of interest** The authors declare no interest conflict. They have no known competing financial interests or personal relationships that could have appeared to influence the work reported in this paper.

**Open Access** This article is licensed under a Creative Commons Attribution 4.0 International License, which permits use, sharing, adaptation, distribution and reproduction in any medium or format, as long as you give appropriate credit to the original author(s) and the source, provide a link to the Creative Commons licence, and indicate if changes were made. The images or other third party material in this article are included in the article's Creative Commons licence, unless indicated otherwise in a credit line to the material. If material is not included in the article's Creative Commons licence and your intended use is not permitted by statutory regulation or exceeds the permitted use, you will need to obtain permission directly from the copyright holder. To view a copy of this licence, visit <http://creativecommons.org/licenses/by/4.0/>.

**Supplementary Information** The online version contains supplementary material available at <https://doi.org/10.1007/s40820-026-02104-z>.

## References

- Z. Liu, H. Fan, T. Guo, Q. Tan, Z. Zhang et al., Ultrasensitive imaging-based sensor unlocked by differential guided-mode resonance. *Nat. Commun.* **16**(1), 6113 (2025). <https://doi.org/10.1038/s41467-025-60947-3>
- E.R. Davies, *Computer and Machine Vision: Theory, Algorithms, Practicalities*. (Academic Press, New York, 2012).
- L. Liu, X. Zhang, Q. Zhang, M. Zhang, X. Zhang et al., Reconfigurable logic of multidimensional encryption based on ReSe<sub>2</sub> homojunction photodetector. *ACS Nano* **19**(27), 25490–25500 (2025). <https://doi.org/10.1021/acsnano.5c08236>
- Z. Wang, T. Wan, S. Ma, Y. Chai, Multidimensional vision sensors for information processing. *Nat. Nanotechnol.* **19**(7), 919–930 (2024). <https://doi.org/10.1038/s41565-024-01665-7>
- H. Huang, X. Liang, Y. Wang, J. Tang, Y. Li et al., Fully integrated multi-mode optoelectronic memristor array for diversified in-sensor computing. *Nat. Nanotechnol.* **20**(1), 93–103 (2025). <https://doi.org/10.1038/s41565-024-01794-z>
- L. Li, J. Kim, C. Jin, G.J. Ye, D.Y. Qiu et al., Direct observation of the layer-dependent electronic structure in phosphorene. *Nat. Nanotechnol.* **12**(1), 21–25 (2017). <https://doi.org/10.1038/nnano.2016.171>
- N. Youngblood, C. Chen, S.J. Koester, M. Li, Waveguide-integrated black phosphorus photodetector with high responsivity and low dark current. *Nat. Photonics* **9**(4), 247–252 (2015). <https://doi.org/10.1038/nphoton.2015.23>
- G. Long, D. Maryenko, J. Shen, S. Xu, J. Hou et al., Achieving ultrahigh carrier mobility in two-dimensional hole gas of black phosphorus. *Nano Lett.* **16**(12), 7768–7773 (2016). <https://doi.org/10.1021/acs.nanolett.6b03951>
- J. Ji, S. Yu, M. Cheng, Y. Mo, Y. Huang et al., Thermally-strained black phosphorus photovoltaics toward spatially-resolved biomimetic vision enhancement. *Adv. Mater.* (2025). <https://doi.org/10.1002/adma.202517056>
- J. Wu, Z. Zhou, J. Sui, Y. Zhang, L. Fang et al., Homojunction-structured 2D black phosphorus optoelectronic device. *Laser Photon. Rev.* **20**(1), e01771 (2026). <https://doi.org/10.1002/lpor.202501771>
- H. Yuan, X. Liu, F. Afshinmanesh, W. Li, G. Xu et al., Polarization-sensitive broadband photodetector using a black phosphorus vertical p-n junction. *Nat. Nanotechnol.* **10**(8), 707–713 (2015). <https://doi.org/10.1038/nnano.2015.112>
- H. Tian, L. Li, M. Ali Mohammad, X. Wang, Y. Yang et al., High-quality reconfigurable black phosphorus p-n junctions. *IEEE Trans. Electron Devices* **65**(11), 5118–5122 (2018). <https://doi.org/10.1109/TED.2018.2869268>
- F. Wang, K. Pei, Y. Li, H. Li, T. Zhai, 2D homojunctions for electronics and optoelectronics. *Adv. Mater.* **33**(15), 2005303 (2021). <https://doi.org/10.1002/adma.202005303>
- Y. Saito, Y. Iwasa, Ambipolar insulator-to-metal transition in black phosphorus by ionic-liquid gating. *ACS Nano* **9**(3), 3192–3198 (2015). <https://doi.org/10.1021/acsnano.5b00497>
- K. Xu, Y. Zhao, Z. Lin, Y. Long, Y. Wang et al., Doping of two-dimensional MoS<sub>2</sub> by high energy ion implantation. *Semicond. Sci. Technol.* **32**(12), 124002 (2017). <https://doi.org/10.1088/1361-6641/aa8ed3>
- J. Jia, S.K. Jang, S. Lai, J. Xu, Y.J. Choi et al., Plasma-treated thickness-controlled two-dimensional black phosphorus and its electronic transport properties. *ACS Nano* **9**(9), 8729–8736 (2015). <https://doi.org/10.1021/acsnano.5b04265>
- X. Yu, S. Zhang, H. Zeng, Q.J. Wang, Lateral black phosphorene P-N junctions formed via chemical doping for high performance



- near-infrared photodetector. *Nano Energy* **25**, 34–41 (2016). <https://doi.org/10.1016/j.nanoen.2016.04.030>
18. G. Wu, X. Wang, Y. Chen, S. Wu, B. Wu et al., MoTe<sub>2</sub> p-n homojunctions defined by ferroelectric polarization. *Adv. Mater.* **32**(16), e1907937 (2020). <https://doi.org/10.1002/adma.201907937>
  19. F. Xue, X. He, J.R.D. Retamal, A. Han, J. Zhang et al., Gate-tunable and multidirection-switchable memristive phenomena in a van der Waals ferroelectric. *Adv. Mater.* **31**(29), 1901300 (2019). <https://doi.org/10.1002/adma.201901300>
  20. S. Wu, G. Wu, X. Wang, Y. Chen, T. Lin et al., A gate-free MoS<sub>2</sub> phototransistor assisted by ferroelectrics. *J. Semicond.* **40**(9), 092002 (2019). <https://doi.org/10.1088/1674-4926/40/9/092002>
  21. L. Tu, R. Cao, X. Wang, Y. Chen, S. Wu et al., Ultrasensitive negative capacitance phototransistors. *Nat. Commun.* **11**(1), 101 (2020). <https://doi.org/10.1038/s41467-019-13769-z>
  22. Y. Huang, Q. Quan, M. Cheng, J. Ji, Y. Mo et al., Unveiling ionic conductive filaments enhanced photovoltaic response exceeding ferroelectrics dimensionality limit. *Adv. Funct. Mater.* e23973 (2025). <https://doi.org/10.1002/adfm.202523973>
  23. S. Wu, Y. Chen, X. Wang, H. Jiao, Q. Zhao et al., Ultra-sensitive polarization-resolved black phosphorus homojunction photodetector defined by ferroelectric domains. *Nat. Commun.* **13**(1), 3198 (2022). <https://doi.org/10.1038/s41467-022-30951-y>
  24. J. Weng, Z. Zhang, T. He, L. Zhang, Y. Zhou et al., WSe<sub>2</sub> pn homojunction photodetector engineered by *in situ* ferroelectric doping. *Adv. Funct. Mater.* **35**(43), 2506469 (2025). <https://doi.org/10.1002/adfm.202506469>
  25. F. Gao, X.Y. Chen, K.B. Yin, S. Dong, Z.F. Ren et al., Visible-light photocatalytic properties of weak magnetic BiFeO<sub>3</sub> nanoparticles. *Adv. Mater.* **19**(19), 2889–2892 (2007). <https://doi.org/10.1002/adma.200602377>
  26. J. Zhao, A. Wang, H. Liu, X. Qi, R. Hao et al., In-plane ferroelectric p/n superstructure photoelectrode for bias-free solar-fuel conversion. *Nano Lett.* **25**(37), 13943–13949 (2025). <https://doi.org/10.1021/acs.nanolett.5c03944>
  27. N. Wang, N. Mao, Z. Wang, X. Yang, X. Zhou et al., Electrochemical delamination of ultralarge few-layer black phosphorus with a hydrogen-free intercalation mechanism. *Adv. Mater.* **33**(1), 2005815 (2021). <https://doi.org/10.1002/adma.202005815>
  28. N. Wang, H. Liu, X. Zhou, Q. Luo, X. Yang et al., Improving harsh environmental stability of few-layer black phosphorus by local charge transfer. *Adv. Funct. Mater.* **32**(34), 2203967 (2022). <https://doi.org/10.1002/adfm.202203967>
  29. F. Xia, H. Wang, Y. Jia, Rediscovering black phosphorus as an anisotropic layered material for optoelectronics and electronics. *Nat. Commun.* **5**, 4458 (2014). <https://doi.org/10.1038/ncomms5458>
  30. J. Jia, J. Xu, J.-H. Park, B.H. Lee, E. Hwang et al., Multifunctional homogeneous lateral black phosphorus junction devices. *Chem. Mater.* **29**(7), 3143–3151 (2017). <https://doi.org/10.1021/acs.chemmater.7b00210>
  31. J. Park, Y. You, D. Lee, J. Kim, Self-powered high-performance WS<sub>2</sub> photodetector *via* a monolithic p-i-n homojunction. *Nano Lett.* **25**(37), 13780–13786 (2025). <https://doi.org/10.1021/acs.nanolett.5c03066>
  32. B. Liu, M. Li, W. Fu, P. Ye, W. E et al., High-performance self-driven ultraviolet photodetector based on SnO<sub>2</sub> p-n homojunction. *Opt. Mater.* **129**, 112571 (2022). <https://doi.org/10.1016/j.optmat.2022.112571>
  33. C. Tan, H. Wang, X. Zhu, W. Gao, H. Li et al., A self-powered photovoltaic photodetector based on a lateral WSe<sub>2</sub>–WSe<sub>2</sub> homojunction. *ACS Appl. Mater. Interfaces* **12**(40), 44934–44942 (2020). <https://doi.org/10.1021/acsami.0c11456>
  34. J. Chen, Z. Zhang, J. Feng, X. Xie, A. Jian et al., 2D InSe self-powered Schottky photodetector with the same metal in asymmetric contacts. *Adv. Mater. Interfaces* **9**(35), 2200075 (2022). <https://doi.org/10.1002/admi.202200075>
  35. J. You, Z. Jin, Y. Li, T. Kang, K. Zhang et al., Epitaxial growth of 1D Te/2D MoSe<sub>2</sub> mixed-dimensional heterostructures for high-efficient self-powered photodetector. *Adv. Funct. Mater.* **34**(10), 2311134 (2024). <https://doi.org/10.1002/adfm.202311134>
  36. K. Shao, H. Nan, R. Qi, C. Jiang, H. Wang et al., Self-powered MoTe<sub>2</sub> homojunction photodetector with ultrafast response *via* h-BN encapsulation and doping regulation. *J. Mater. Chem. C* **13**(36), 18972–18980 (2025). <https://doi.org/10.1039/D5TC02340H>

**Publisher's Note** Springer Nature remains neutral with regard to jurisdictional claims in published maps and institutional affiliations.